Large longitudinal spin alignment generated in inelastic nuclear reactions

D. E. M. Hoff,[1,*] G. Potel,[2] K. W. Brown,[1,†] R. J. Charity,[1] C. D. Pruitt,[1] L. G. Sobotka,[1] T. B. Webb,[1] B. Roeder,[3] and A. Saastamoinen[3]

[1]*Departments of Chemistry and Physics, Washington University, St. Louis, Missouri 63130, USA*

[2]*National Superconducting Cyclotron Laboratory, Michigan State University, East Lansing, Michigan 48824, USA*

[3]*Cyclotron Institute, Texas A&M University, College Station, Texas 77840, USA*

(Received 25 March 2018; published 17 May 2018)

Large longitudinal spin alignment of $E/A = 24$ MeV ^{7}Li projectiles inelastically excited by Be, C, and Al targets was observed when the latter remain in their ground state. This alignment is a consequence of an angular-momentum-excitation-energy mismatch, which is well described by a DWBA cluster-model ($\alpha + t$). The longitudinal alignment of several other systems is also well described by DWBA calculations, including one where a cluster model is inappropriate, demonstrating that the alignment mechanism is a more general phenomenon. Predictions are made for inelastic excitation of ^{12}C for beam energies above and below the mismatch threshold.

DOI: 10.1103/PhysRevC.97.054605

I. INTRODUCTION

The generation and manipulation of nuclear spin alignment or polarization has led to many applications in physics. In nuclear physics, the production of polarized beams has enabled vector and tensor analyzing power measurements [1]. Theoretical predictions of these quantities are sensitive to the spin-spin and spin-orbit coupling derived from the effective nucleon-nucleon (NN) and 3N forces used, so these studies can put a constraint on the effective potentials. Spin alignment generated in nuclear reactions can give insight into the underlying reaction mechanisms [2,3], and has also been utilized for g-factor measurements, which elucidate nuclear wave functions used to understand nuclear structure [4,5].

Methods for measuring the spin alignment of excited nuclei are dependent on the nuclear state of interest and its decay mode. For bound excited states, the population of magnetic substates (and thus the spin alignment/polarization) can be measured by analyzing the angular distribution of an emitted γ ray [6–12]. However, for unbound excited states, the angular correlations of the sequential breakup fragments can be measured to determine the final magnetic substate distribution [13,14], which is the approach taken in this work.

The motivation for this study comes from the observation of large longitudinal spin alignment of inelastically excited ^{7}Be* projectiles scattered off a ^{9}Be target [13]. In that work, the proposed mechanism for generating spin alignment evoked the unusual molecular structure of the ^{9}Be target. However, subsequently large longitudinal alignment of ^{7}Li* was observed with Be, C, and Al targets [14]. This observation prompted the search for a more general mechanism. Such a mechanism does exist and originates from an angular-momentum-excitation-energy mismatch that forces the exit-channel reaction plane to tilt to conserve angular momentum [14]. This mechanism is reminiscent of Brink's condition for optimal nucleon transfer stemming from angular momentum conservation [15]. For this mismatch to occur, the excitation energy of the projectile must be small compared to the beam energy. This alignment mechanism is independent of the scattering partner (and thus scattering potential), and as a consequence, it should be possible to find large longitudinal alignment in many nuclear systems.

Our previous letter on this alignment mechanism focused on the ^{7}Li + ^{12}C system [14]. The present work presents the data for all three targets. The details of the experiment are discussed in Sec. II and the results are presented in Sec. III. The theory behind the DWBA calculations and the resulting alignment mechanism are presented in Sec. IV. An optical-model analysis was carried out for the ^{7}Li + ^{12}C reaction using the arguments of Sec. IV, and the results of this analysis are presented in Sec. V. The effect of spin-orbit coupling on the observed alignment is also discussed in Sec. V. Other reaction examples where we believe this mechanism has been active are mentioned in Sec. VI. Also included in Sec. VI are predictions for the ^{12}C + ^{12}C system.

II. EXPERIMENTAL METHOD

The Texas A&M K-500 Cyclotron provided an $E/A = 24.0$ MeV ^{7}Li beam that impinged on targets of ^{9}Be, ^{12}C, and ^{27}Al with thicknesses of 9.47, 9.60, and 10.38 mg/cm^{2}, respectively. The breakup fragments of ^{7}Li ($\alpha + t$) were detected by two annular Si-CsI(Tl) telescopes, one looking through the hole of the other, mounted on a rail parallel to the beam axis. A schematic of the experimental setup is shown in Fig. 1. The upstream telescope contained an 85-mm-diameter (3-cm-diameter hole) segmented annular Si (32 rings and 48 pie-shaped sectors) placed 15 cm from the target position.

*dhoff@go.wustl.edu

†Present Address: National Superconducting Cyclotron Laboratory, Departments of Physics and Astronomy, Michigan State University, East Lansing, MI 48824.

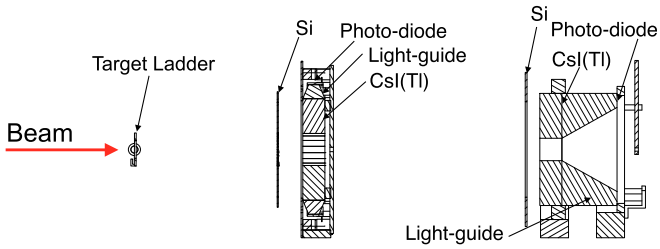

FIG. 1. A schematic of the detector setup consisting of two Si-CsI(Tl) telescopes. The first telescope was placed 15 cm, and the second 36 cm, downstream of the target position.

The downstream telescope contained a 70-mm-diameter (22-mm-diameter hole) segmented annular Si (48 incomplete rings and 16 pie-shaped sectors) placed 36 cm from the target position. For each telescope, the Si detector were backed by 16 2-cm-thick CsI(Tl) crystals, which were used to measure the residual energies of the decay fragments and, in conjunction with the Si detector, to determine the particle type.

Energy calibrations for the CsI(Tl) detectors were performed with proton, deuteron, and α beams at several energies. These beams impinged upon a thin Au target and several Al targets of varying thicknesses, giving different degraded energies. A summary of the calibration beams, degraders, and resulting energies is shown in Table I. The degraded energies were determined from SRIM energy-loss tables [16]. The energy calibrations determined for the deuterons were used for tritons.

For the downstream telescope, angle-independent CsI(Tl) calibrations were found for deuterons and alphas. On the upstream telescope, the photo-diode readouts of the scintillated light were placed on the outside radius of the CsI(Tl) crystals (Fig. 1). This external radial readout introduced nonuniform light collection that depended on the polar angle of the energy deposition in the CsI(Tl) crystal. To correct for this, energy calibrations were performed as a function of polar angle, taking into account the effective degrader thickness and kinematic effects, by gating on eight different regions of polar angle as determined by the Si detector.

Energy calibrations for the Si detectors were performed with a mixed α source of ^{148}Gd, ^{239}Pa, ^{241}Am, and ^{244}Cm. For the downstream Si detector, the α calibrations were sufficient,

TABLE I. Calibration beams and the energies generated with the degraders.

Species	Energy [MeV/A]	Target	Thickness [mg/cm^2]	Degraded energy [MeV/A]
p	24.2	Au	20.0	24.0
		Al	429	15.8
d	24.2	Au	20.0	24.1
		Al	429	20.3
		Al	858	15.8
	12.0	Au	20.0	11.9
α	24.0	Au	20.0	23.8
		Al	429	15.6

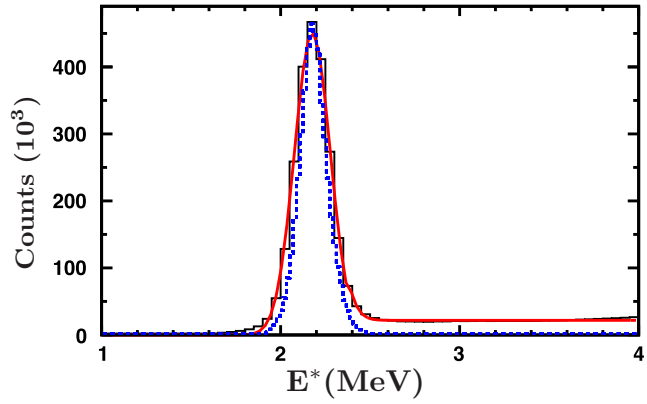

FIG. 2. The invariant-mass spectrum for $\alpha + d$ events showing the first particle-unbound state of ^{6}Li. The solid red line is a fit to the measured distribution, shown by the histogram, with the background modeled by a Fermi function. The dashed blue line is the expected experimental resolution from Monte Carlo simulations.

however, they were not sufficient for the upstream Si detector either due to a nonuniform dead layer or an incomplete depletion region. Therefore, the upstream Si detector was used solely for determination of the scattering angle and particle identification. The energy lost in the upstream Si was determined from the energy deposited in the CsI(Tl) and SRIM [16] energy-loss tables.

To check the robustness of the energy calibrations, an invariant-mass reconstruction was made for $\alpha + d$ events, and the spectrum is shown in Fig. 2. The width of the first particle-unbound state in ^{6}Li at 2.185 MeV is 24 keV, much smaller than the experimental resolution, so the measured width of this state is a good indicator of the intrinsic resolution of the detector system. The solid red line in Fig. 2 is a fit to the measured distribution using a Fermi function to model the background. The centroid of this fit is 2.177 MeV, with a FWHM of 235 keV. The measured width is a little larger than predictions from Monte Carlo simulations of the detector system, shown as the blue dashed line in Fig. 2. The discrepancy is most likely due to imperfect energy calibrations.

III. EXPERIMENTAL RESULTS

Figure 3(a) shows the $\alpha + t$ invariant-mass spectrum for all targets. The first two particle-unbound states of ^{7}Li (at $E^* =$ 4.63 and 6.68 MeV, respectively) are clearly seen.

To ensure that only events where ^{7}Li is excited to the 4.63 MeV ($J^\pi = 7/2^-$) state were considered in the magnetic substate extraction, the gate G1, shown in Fig. 3(a), was applied. After reconstructing the ^{7}Li momentum, the targets' excitation energy was deduced from two-body kinematics. These excitation energy distributions are shown for the C, Be, and Al targets in Figs. 3(b)–3(d), respectively. The dashed red lines correspond to energy levels in the respective nuclei. The large separation between the ground and first excited state of ^{12}C (4.44 MeV, $J^\pi = 2^+$) allowed a clean selection of the ground state (via gate G2) without contributions from excited states. The energy resolution of the detector system was insufficient to separate the ground and first excited state of ^{9}Be

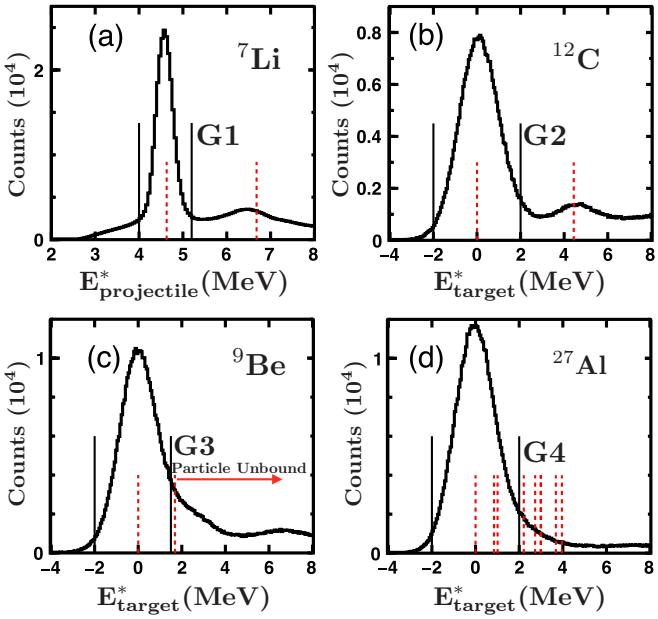

FIG. 3. (a) The excitation energy distribution for ^{7}Li, summed from all three targets. The gate employed to select the $J^\pi = 7/2^-$ state is indicated. The ^{12}C, ^{9}Be, and ^{27}Al target excitation energy distributions after selecting ^{7}Li excited to the 4.63 MeV ($J^\pi = 7/2^-$) state are shown in (b), (c), and (d), respectively. The dashed vertical red lines correspond to energy levels for the respective nuclei.

(1.68 MeV, $J^\pi = 1/2^+$). Nevertheless, a tight gate on the ^{9}Be ground state peak, shown as G3 in Fig. 3(c), can be used to bias the dataset with events where ^{9}Be remains in its ground state. In the case of Al, there are many low-lying excited states, and these can be observed as the long tail in the reconstructed ^{27}Al excitation energy distribution. Subsequently presented spectra are gated on the target "ground-state" peak by requiring the reconstructed target excitation energy to fall within the indicated G2, G3, or G4 gates.

Monte Carlo simulations were also used to understand the geometrical efficiency of the detector array. An example of the simulated geometrical efficiency is shown for the ^{7}Li + ^{12}C system in Fig. 4(a). The angle ψ is defined as the angle of the breakup with respect to the beam axis, which is also our quantization axis. The angle χ is measured from the reconstructed scattering plane. A diagram defining these angles is provided in Fig. 4(b). The efficiency-corrected angular correlations for the decay of ^{7}Li* projectiles, after interaction with C, Be, and Al targets, are shown in Figs. 4(c)–4(e), respectively. The resulting angular correlations are all very similar with preferred fragment emission transverse to the beam [$\cos(\psi) = 0$]. This result is consistent with the prior study using a beam of ^{7}Be at $E/A = 65.5$ MeV [13]. The projections of the angular correlations and the associated Legendre-polynomial-squared fits to the data are shown in Figs. 4(f)–4(h). The asymmetry in the $\cos(\psi)$ distributions is likely due to imperfect energy calibrations. This was determined by introducing a small linear shift to the assigned energies of the tritons in the Monte Carlo simulations which reproduced the observed asymmetries. The magnetic-substate distributions of ^{7}Li* extracted from the angular correlations are shown in Figs. 4(i)–4(k) for the three targets.

The magnitude of alignment can be quantified by a scalar conventionally denoted by $\mathcal{A}$ (sometimes called P_{zz}) that incorporates the population of specific magnetic substates. Given a quantization axis, the scalar can be defined as

$$\mathcal{A} = \sum_{m_f} \frac{3m_f^2 - J(J+1)}{J(2J-1)} \rho^J_{m_f,m_f}. \tag{1}$$

The magnetic substate populations are denoted in this work by the diagonal density matrix elements of the final state, $\rho^J_{m_f,m_f}$. The formulation of the density matrix for sequential breakup can be found in Ref. [13]. For ^{7}Li* inelastically excited to the $J^\pi = 7/2^-$ state, the magnitude of longitudinal alignment was found to be $\mathcal{A} = 0.49(1), 0.53(1), 0.53(1)$ after scattering off C, Be, and Al nuclei, respectively. This magnitude of alignment for ^{7}Li* is quite large compared to other types of reactions at similar energies. For example, longitudinal spin alignment has been observed in several projectile fragmentation experiments [17,18], but the level of alignment produced varies drastically. In the production of ^{32}Al from projectile fragmentation, the alignment was found to be $\mathcal{A} = 0.08$. The population of the $J^\pi = 19/2^-$ high spin isomer of ^{43m}Sc, produced by projectile fragmentation, yielded an alignment $\mathcal{A} = 0.35$. The similarity of the alignment found for ^{7}Li in this work, for each target, requires an explanation, and this is provided in the following section.

IV. THEORY

The longitudinal alignment arising from an angular-momentum-excitation-energy mismatch should be present in any single inelastic process X(Y,Y*)X or X(Y,Y)X*, provided the excitation energy is sufficiently small compared the beam energy. A change in intrinsic spin must be accommodated for by one or more different processes: a change between the incoming and outgoing orbital angular momenta (either a reduction in magnitude or tilting [6,14]), a coupling of the fragment spins and the incoming orbital momentum (i.e., spin-orbit effects [19]), or some other spin-spin interaction.

A. Semiclassical argument for an angular-momentum-excitaiton-energy mismatch

For sufficiently large energies, the mechanism for generating longitudinal spin alignment can be understood classically, where a loss of center-of-mass kinetic energy directly corresponds to a change in magnitude of the reaction orbital angular momentum, ΔL, assuming a fixed radius of interaction, R. Repeating the analysis in Ref. [14], an upper limit on the possible transfer of reaction orbital angular momentum can be found by assuming $\mathbf{p}_{\rm in}, \mathbf{p}_{\rm out} \perp \mathbf{R}$. This gives the Newtonian result,

$$\Delta L = R\sqrt{2\mu E_{\rm c.m.}}\left(1 - \sqrt{1 - \frac{E^*}{E_{\rm c.m.}}}\right), \tag{2}$$

where μ is the reduced mass of the system, and $E_{\rm c.m.}$ is the kinetic energy in the center-of-mass frame. Applying

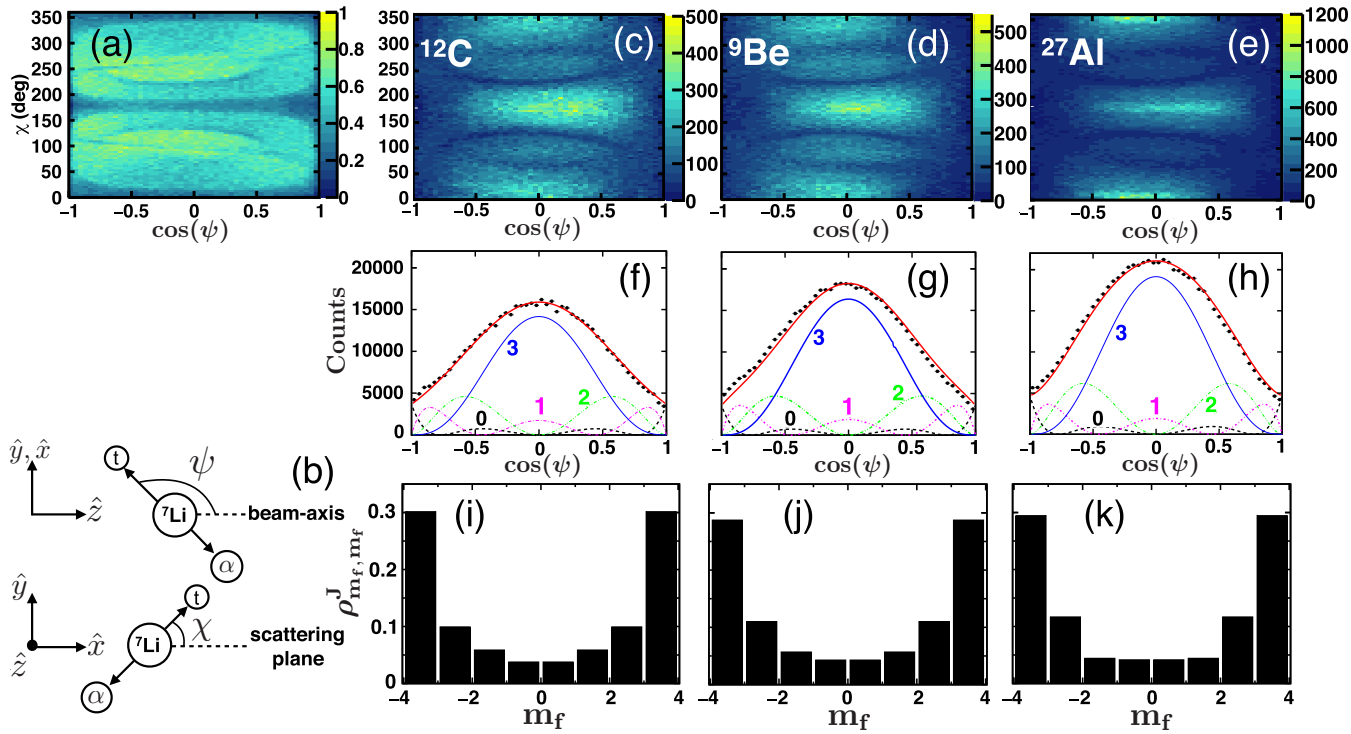

FIG. 4. (a) The geometrical efficiency of the detector system determined from Monte Carlo simulations for the ^{12}C target system. (b) A diagram of the angles ψ and χ used for the correlations. The efficiency-corrected angular correlations for the breakup of ^{7}Li* after interacting with (c) C, (d) Be, and (e) Al targets over the measured angular range; (f, g, h) the projections of the angular correlations onto the cos(ψ) axis; and (i, j, k) the extracted magnetic-substate distributions of ^{7}Li* with the separate targets, respectively. All data have been gated on the ground-state peak of the respective target nucleus.

this equation to the studied $^{7}\mathrm{Li} + {}^{12}\mathrm{C}$ system by using an excitation energy of $E^{*} = 4.63$ MeV, a beam energy of $E/A = 24.0$ MeV, and a radius of $R = 5$ fm, one finds $\Delta L < 1\hbar$. This means a change in magnitude of the reaction orbital angular momentum alone cannot excite ^{7}Li to the 4.63 MeV state, as the excitation requires a change in intrinsic spin of $2\hbar$. When the center-of-mass energy is much larger than the excitation energy, $E_{\mathrm{c.m.}} \gg E^{*}$, L must tilt to conserve angular momentum when there is a change in spin of the reactant (in the absence of a spin flip of either reactant). As a result the final reaction angular momentum is likely to have a finite projection, M, on the beam axis. This argument for an angular-momentum-excitation-energy mismatch suggests this phenomenon is a threshold effect. As one increases the beam energy (i.e., $E_{\mathrm{c.m.}}$), the mismatch becomes greater.

B. Constructing the transition amplitude for inelastic processes

To probe the connection between the final projection of L and the inelastic excitation, it is useful to look at the transition amplitude, or T matrix, which gives the probability of going from an initial magnetic substate, m_i, to a final magnetic substate, m_f. Ultimately, it will be shown that the final projection of L is related to the change in fragment spin by $M = m_f - m_i$. By integrating the squared T matrix over a given angular region (and summing over the initial states because the beam is unpolarized), one can predict the final outcome of the magnetic-substate distribution for an exit-channel fragment in the reaction.

To construct the T matrix for the inelastic processes of interest, we assume a general form for the projectile-target interaction. It should be able to induce multipolar excitations of the projectile by coupling the projectile-target relative motion, described with the vector $\mathbf{R}$, with the internal degrees of freedom of the projectile, described with some intrinsic coordinate $\boldsymbol{\xi}$. The interaction

$$\Delta(\mathbf{R},\boldsymbol{\xi}) = 4\pi \sum_{K} \frac{(-1)^{K}}{\sqrt{2K+1}} \Delta_{K}(R,\xi)[Y^{K}(\hat{\xi})Y^{K}(\hat{R})]^{0}_{0} \quad (3)$$

satisfies the above requirement and is rotationally invariant. The square brackets denote angular momentum coupling, where $[Y^{p_1}Y^{p_2}]^{P}_{M_P} = \sum_{m_1,m_2} \langle p_1 m_1 p_2 m_2 | P M_P \rangle Y^{p_1}_{m_1} Y^{p_2}_{m_2}$. The requirement that $P = 0$ and $M_P = 0$ generates a scalar that only depends on the angle between $\boldsymbol{\xi}$ and $\mathbf{R}$. The actual form of the Δ functions will depend on the case under consideration and, more specifically, on the model used to describe inelastic excitation.

Focusing on breakup experiments, the population of the particle-unbound resonance is described as an inelastic excitation of the fragment-core system in terms of the relative coordinate $\mathbf{r}$. This can be easily extended to cluster-model calculations, provided the fragment is treated as a nucleus instead of a nucleon. We define the model interaction (using p-t, f-t, and c-t as projectile-target, fragment-target, and

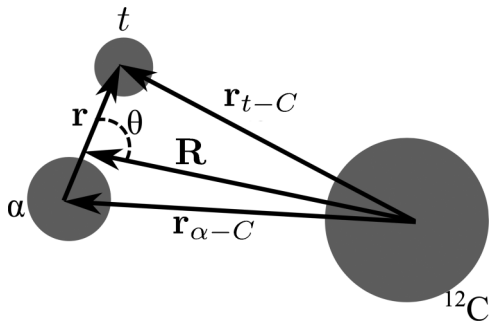

FIG. 5. The coordinates **r** and **R** as well as the fragment-target and core-target coordinates for the ^{7}Li + ^{12}C system.

core-target, respectively),

$$\Delta(R,r_{c\text{-}t},r_{f\text{-}t}) = U_{p\text{-}t}(R) - U_{c\text{-}t}(r_{c\text{-}t}) - U_{f\text{-}t}(r_{f\text{-}t}), \quad (4)$$

where these effective interactions are taken as central phenomenological optical potentials. This transition potential can be cast into the general form of Eq. (3),

$$\Delta(R,r_{c-t},r_{f-t}) = \sum_K \Delta_K(R,r)P_K(\theta) = 4\pi \sum_K \frac{(-1)^K}{\sqrt{2K+1}} \times \Delta_K(R,r)[Y^K(\hat{r})Y^K(\hat{R})]^0_0, \quad (5)$$

where θ is the angle between **r** and **R** (diagrammed in Fig. 5), $P_K(\theta)$ are the Legendre polynomials. The multipole components $\Delta_K(R,r)$ can be computed from the interaction Eq. (4),

$$\Delta_K(R,r) = \frac{2K+1}{2}\int_0^\pi \Delta(R,r_{c\text{-}t},r_{f\text{-}t})P_K(\theta)\sin\theta\, d\theta. \quad (6)$$

The population of the resonance is modeled as a direct, one-step inelastic excitation of the fragment-core system. The cross section is proportional to the squared modulus of the transition amplitude T_{m_i,m_f}, which is calculated in the distorted wave Born approximation (DWBA).

The distorted waves describing the relative projectile-target motion in the initial $[\chi_{i,m_i}(\mathbf{R},\mathbf{k}_i)]$ and final $[\chi_{f,m_f}(\mathbf{R},\mathbf{k}_f)]$ channels are solutions of the phenomenological central optical potential $U_{p\text{-}t}(R)$ used in Eq. (4). Note that, to avoid complications inherent in the treatment of the continuum, the final particle-unbound state is modeled with a very weakly bound wave function (quasibound approximation). With these ingredients the T matrix is

$$T_{m_i,m_f} = \int \chi^{(-)*}_f(\mathbf{R},\mathbf{k}_i)\phi^*_{f,m_f}(\mathbf{r})\Delta(R,r_{c-t},r_{f-t}) \times \chi^{(+)}_i(\mathbf{R},\mathbf{k}_f)\phi_{i,m_i}(\mathbf{r})\, d\mathbf{r}\, d\mathbf{R}, \quad (7)$$

and the differential cross section for a specific $m_i \to m_f$ transition is

$$\frac{d\sigma}{d\Omega}(\theta_{\text{c.m.}};m_i,m_f) = \frac{k_f}{k_i}\frac{\mu^2}{4\pi^2\hbar^4}\left|T_{m_i,m_f}\right|^2. \quad (8)$$

In the last expression, $\theta_{\text{c.m.}}$ is the scattering angle in the center-of-mass frame. For the sake of numerical computation, but also to gain further insight, it is convenient to work out the partial wave analysis of Eq. (7). We thus write down the standard expressions of the scattering and bound wave functions in terms of a spherical harmonics series,

$$\chi^{(+)}_i(\mathbf{R};\mathbf{k}_i) = \frac{4\pi}{k_i R}\sum_{L_i} i^{L_i}e^{i\sigma_i^{L_i}} f_{L_i}(R)\sqrt{2L_i+1} \times [Y^{L_i}(\hat{R})Y^{L_i}(\hat{k}_i)]^0_0, \quad (9)$$

$$\chi^{(-)*}_f(\mathbf{R};\mathbf{k}_f) = \frac{4\pi}{k_f R}\sum_{L_f} i^{-L_f}e^{i\sigma_f^{L_f}} g_{L_f}(R)\sqrt{2L_f+1} \times [Y^{L_f}(\hat{R})Y^{L_f}(\hat{k}_f)]^0_0, \quad (10)$$

$$\phi_{i,m_i}(\mathbf{r}) = u_i(r)\sum_{\mu_i,m_{\text{frag}}} \langle \ell_i\ \mu_i\ J_{\text{frag}}\ m_{\text{frag}}|J_i\ m_i\rangle \times Y^{\ell_i}_{\mu_i}(\hat{r})\Xi_{m_s}(\sigma), \quad (11)$$

$$\phi^*_{f,m_f}(\mathbf{r}) = u_f(r)\sum_{\mu_f,m_{\text{frag}}} \langle \ell_f\ \mu_f\ J_{\text{frag}}\ m_{\text{frag}}|J_f\ m_f\rangle \times Y^{\ell_f}_{\mu_f}(\hat{r})(-1)^{\mu_f}\Xi^\dagger_{m_s}(\sigma). \quad (12)$$

The radial wave functions $u_i(r)$ and $u_f(r)$ are computed with a simple Woods-Saxon potential which reproduces the particle-emission threshold. The functions $f_{L_i}(R)$ and $g_{L_f}(R)$ are the solutions of the radial Schrödinger equation for the potential $U_{p\text{-}t}(R)$ in the initial and final channel, respectively, and $\sigma_i^{L_i}$,$\sigma_f^{L_f}$ are the corresponding Coulomb phase shifts. The spinors $\Xi_{m_s}(\sigma)$ describe the spin degrees of freedom. Since all the interactions we are considering are spin-independent, the spin projection m_{frag} remains unchanged during the collision process, while the employed version of Δ and the partial wave expansion enforces angular momentum conservation. We define the transition density for a multipolarity K,

$$\rho_K(R) = \int u_i(r)\,u_f(r)\Delta_K(R,r)r^2\,dr. \quad (13)$$

Using Eqs. (9)–(13) in Eq. (7), and after some algebra, we obtain

$$T_{m_i,m_f} = \sum_{K,L_i,L_f}\langle L_i\ 0\ K\ M|L_f\ M\rangle\langle J_i\ m_i\ K\ M|J_f\ m_f\rangle \times Y^{L_f}_{-M}(\hat{k}_f)I(K,L_i,L_f), \quad (14)$$

with $I(K,L_i,L_f)$ defined as,

$$I(K,L_i,L_f) = 2\pi^{1/2}i^{L_i-L_f}e^{i(\sigma_i^{L_i}+\sigma_i^{L_f})} \times (2L_i+1)^{3/2}(2K+1)(2\ell_i+1) \times \sqrt{(2J_i+1)(2\ell_f+1)}\begin{Bmatrix}\ell_i & J_{\text{frag}} & J_i\\ J_f & K & \ell_f\end{Bmatrix} \times \langle L_i\ 0\ K\ 0|L_f\ 0\rangle\langle \ell_i\ 0\ K\ 0|\ell_f\ 0\rangle, \times \int f_{L_i}(R)\,g_{L_f}(R)\rho_K(R)\,dR. \quad (15)$$

C. Properties of the transition amplitude

Partial waves, or L waves, are semiclassically related to the impact parameter, b, which characterizes the distance of

closest approach for the projectile's trajectory. The relationship between these two parameters is given by $L = p_\infty b$, where p_∞ is the momentum of the particle at far distances, or rather the momentum of the beam in scattering experiments. Small impact parameters, and thus small L, represent head-on collisions that result in processes such as fusion and projectile/target fragmentation. Larger impact parameters give rise to transfer and inelastic scattering before giving way to pure Coulomb scattering at even larger impact parameters.

If the beam energy and/or the reduced mass of the colliding systems is large, the process is rather well localized in space. Due to the absorptive nature of the optical potential, the main contribution to the inelastic process comes from the nuclear surfaces (peripheral collisions). In this situation, the partial waves contributing to the cross section are large compared to the multipolarity of the transition and are narrowly peaked around the grazing angular momentum, $L_{\rm graz} \gg K$. Here we define the grazing angular momentum by the touching spheres approximation with $L_{\rm graz} = p_\infty r_{\rm graz}$, where the grazing radius is given by $r_{\rm graz} = 0.5$ fm $+ (1.36$ fm$)(A_p^{1/3} + A_t^{1/3})$ [20]. Above the grazing angular momentum, the partial wave contribution to the total reaction cross sections drops steeply.

Assuming there is one dominant multipolarity, K', and if only processes where $L_i = L_f$ are considered (employing the angular-momentum-excitation-energy matching argument) we can take advantage of the fact that as $L \to \infty$ the first Clebsch-Gordan coefficient in Eq. (14) is independent of L. Since only L around $L_{\rm graz}$, which is large at intermediate energies, will contribute to the cross section, the Clebsch-Gordan coefficients in Eq. (14) can be factored out resulting in the expression,

$$T_{m_i,m_f} \approx \langle L_{\rm graz}\ 0\ K'\ M | L_{\rm graz}\ M\rangle\ \langle J_i\ m_i\ K'\ M | J_f\ m_f\rangle \times \sum_L Y^L_{-M}(\hat{k}_f) I(K',L,L). \quad (16)$$

The angle dependence and implicit energy dependence of the T matrix is represented in the sum over L in Eq. (16).

Oscillations in alignment with angle are expected from the high-order spherical harmonics required for the target-projectile motion in the wave function, although, at larger angles the alignment should become fairly constant. This is due to the mixing of several L waves about $L_{\rm graz}$, which is taken into account by the sum, $\sum_L Y^L_{-M}(\hat{k_f}) I(K',L,L)$, in Eq. 16. If the angle dependence of the T matrix is integrated over (i.e., angle averaged), then the magnetic-substate distribution of inelastically excited species should show large longitudinal alignment at beam energies above the mismatch threshold, when the reaction partner remains in its ground state. In fact, the observed alignment should be very similar to the Clebsch-Gordan coefficients presented in Eq. (16).

V. OPTICAL-MODEL ANALYSIS OF ^{7}Li + ^{12}C

The DWBA breakup calculations outlined in Sec. IV were performed for the ^{7}Li + ^{12}C system using FRESCO [21], assuming an $\alpha + t$ cluster structure of ^{7}Li. The optical potentials used were obtained from a fit of the relative elastic and inelastic scattering angular distributions, as well as the angular correlations for the breakup of ^{7}Li* [4.63 MeV] shown in Fig. 4.

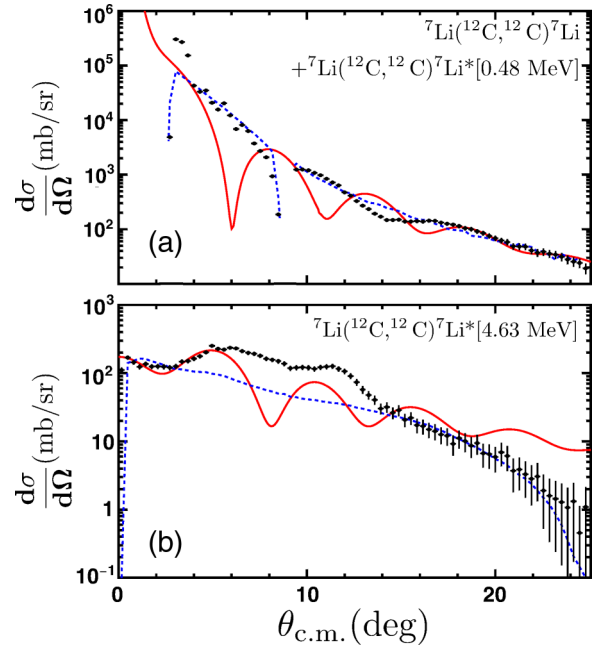

FIG. 6. Data (black circles) and DWBA predictions (solid red lines) for the ^{7}Li + ^{12}C system: (a) elastic scattering and the single inelastic excitation of ^{7}Li to the 0.48 MeV state and (b) the single inelastic excitation of ^{7}Li to the 4.63 MeV state. The predicted angular distributions were used as inputs into the Monte Carlo simulations of the detector system and the expected detector distributions are compared to the data (blue dashed lines).

Absolute cross sections were not available from our measurements, and so the relative cross section data [black circles in Figs. 6(a) and 6(b)] were scaled to the DWBA predictions in the fitting procedure. The volume terms for the phenomenological optical potentials are described by a Woods-Saxon form, while the spin-orbit coupling uses a differential Woods-Saxon form. The radii of the potentials follow the form $r = r_0(A_1^{1/3} + A_2^{1/3})$, where A_1 and A_2 are the mass numbers for the nuclei in the system and r_0 is specified separately for the real and imaginary potentials. The initial α-^{12}C effective interaction was obtained from [22] and the magnitude of the interaction was allowed to vary in fitting. The t-^{12}C potential was extrapolated from a ^{3}He-^{12}C effective interaction. The α-t and ^{7}Li-^{12}C potential parameters were allowed to vary during the fitting procedure, as well as the spin-orbit coupling of ^{7}Li. The fitted potential parameters are listed in the Table II and the resulting fits to the elastic and single inelastic excitation cross sections of ^{7}Li are shown in Figs. 6(a) and 6(b) as the solid red lines.

The predicted angular distributions were then used as inputs into the Monte Carlo simulations, which take into account a tilt of the beam axis with respect to the detector axis of 0.62°, a beam divergence characterized by a two-dimensional Gaussian with $\sigma_Y = 1.53°$ and $\sigma_X = 0.32°$, and a beam spot size 4 mm in diameter at the target. The tilt with respect to the beam axis was determined from Monte Carlo simulations by rotating the beam in the simulation until the experimental hit-map of elastic scattering events was reproduced. The divergence parameters were calculated from LISE++ simulations of the

TABLE II. Fitted optical potential parameters for the ^{7}Li + ^{12}C DWBA calculations, assuming a cluster model for ^{7}Li ($\alpha + t$). The volume terms use a Woods-Saxon form. The spin-orbit coupling uses a differential Woods-Saxon form.

System	Type	V [MeV]	r_{real} [fm]	a_{real} [fm]	W [MeV]	r_{imag} [fm]	a_{imag} [fm]
^{7}Li-^{12}C	Volume	169.4	1.28	0.800	34.8	1.67	0.758
	Spin-Orbit	0.550	1.48	0.727	0.720	1.48	0.485
α-^{12}C	Volume	72.0	1.43	0.692	32.0	1.43	0.692
t-^{12}C	Volume	65.3	1.15	0.400	30.9	1.35	0.407
α-t	Volume	71.6	1.20	0.736			

several quadrupole and dipole magnet settings used to tune the beam [23]. The beam was tuned through a 4-mm-diameter hole in a target blank covered in scintillator. By minimizing the amount of scintillated light viewed by a camera, the beam spot size at the target position was constrained. These combined features of the ^{7}Li beam severely limited the scattering angle resolution, and the expected measured distributions are shown as the blue dashed lines in Figs. 6(a) and 6(b).

The reactions of interest, single inelastic excitations, are well described by peripheral collisions with large orbital angular momentum between the projectile and target. The solid black line in Fig. 7 shows the contributions to the total reaction cross section of each $\mathcal{J}$, where $\mathcal{J}$ is the addition of L and incoming spin of the projectile, for $E/A = 24$ MeV ^{7}Li interacting with ^{12}C from a DWBA cluster-model calculation. The dashed red line in Fig. 7 shows the partial cross section as a function of $\mathcal{J}$ for the inelastic excitation of interest, where ^{7}Li is excited to the $E^{*} = 4.63$ MeV ($J^{\pi} = 7/2^{-}$) state while the target remains in its ground state.

As can be seen in Fig. 7, the inelastic excitation of interest occurs at very large $\mathcal{J}$ corresponding to a peripheral reaction

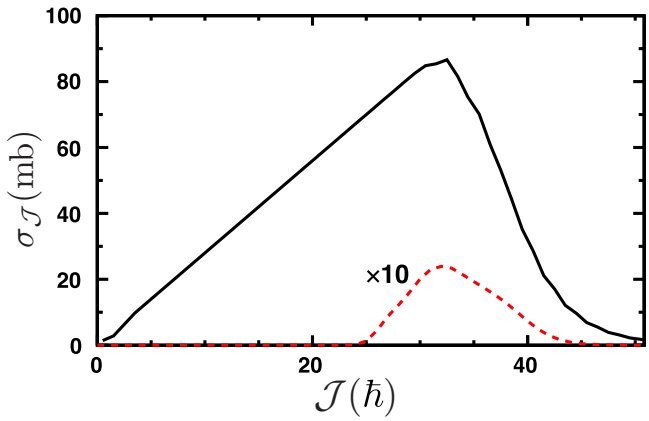

FIG. 7. The partial cross section as a function of $\mathcal{J}$ for the total reaction cross section of the system $E/A = 24$ MeV ^{7}Li + ^{12}C using DWBA calculations (solid black line) and for the inelastic excitation of ^{7}Li to the 4.63 MeV excited state while the target remains in its ground state (dashed red line). The inelastic cross section has been scaled by a factor of 10 for comparison.

(i.e., is near $L_{\text{graz}} = 35\hbar$). The DWBA cluster-model calculations indicate that this particular inelastic excitation of ^{7}Li takes up a relatively small part of the overall reaction cross section. The calculations also suggest that the inelastic excitation of ^{7}Li studied is a purely nuclear process. This is consistent with relativistically correct calculations of the Coulomb excitation cross section [14].

A. Spin-orbit effects on alignment

When spin-orbit effects are introduced to the effective potential spin-flip processes become possible. These spin-flips are accompanied by a tilt of the orbit between the projectile and target [19]. This spin-orbit tilting can potentially diminish or destroy the overall alignment generated from an angular-momentum-excitation-energy mismatch. This should be a miniscule effect due to the typically small coupling strength of the spin-orbit potential. However, small spin-orbit couplings can have a large effect on the resulting angular correlations. Figure 8(a) shows the predicted ψ-χ correlations from a DWBA cluster-model calculation for inelastically excited ^{7}Li* [4.63 MeV] after interacting with a ^{12}C target, at a beam energy of $E/A = 24$ MeV, with no spin-orbit potential (in the angular range of $3^{\circ} < \theta_{\text{c.m.}} < 23^{\circ}$). The pattern of the calculated correlations is very similar to the data [Fig. 8(e)] although the centroid of the central ridge is shifted to negative $\cos(\psi)$ values, as opposed to the positive values in the experiment. It was found that the the inclusion of a small complex spin-orbit coupling for the projectile resulted in an angular correlation pattern [Fig. 8(b)] much more consistent with the data. Small spin-orbit couplings do not affect the alignment (i.e., the magnetic-substate distribution). Increasing the real spin-orbit coupling strength to $V_{\text{SO}} = 3.0$ MeV distorts the angular correlations but also preserves the alignment [Fig. 8(c)]. The angular correlations, and differential cross sections, are even more sensitive to further increases of the complex spin-orbit strength. Figure 8(d) shows the predicted correlations with $W_{\text{SO}} = 1.44$ MeV, at which point the pattern of the correlations is completely distorted and the longitudinal alignment is destroyed. In fact, larger increases of W_{SO} result in spin alignment transverse to the beam axis. This study suggests that angular correlation measurements, in concordance with differential cross section data, can put a constraint on the strength of spin-orbit effects in reactions. These constraints are analogous to those made by analyzing power measurements [1]. However, these alignment effects do not require a polarized beam.

VI. OTHER CASES FOR LARGE LONGITUDINAL SPIN ALIGNMENT

Large longitudinal spin alignments were observed in the inelastic excitation of ^{7}Be and ^{6}Li to particle-decaying states [13]. ^{6}Li is modeled well by an $\alpha + d$, and ^{7}Be by an $\alpha + ^{3}$He, cluster structure, so the manifestation of this alignment mechanism in the cluster-model directly applies to these nuclei. Another example for this large longitudinal spin alignment is the inelastic excitation of ^{17}Ne to the 1.76 MeV state ($J^{\pi} = 5/2^{-}$), which subsequently $2p$ decays to ^{15}O. The decay is purely sequential, and in the first step, ^{17}Ne decays directly

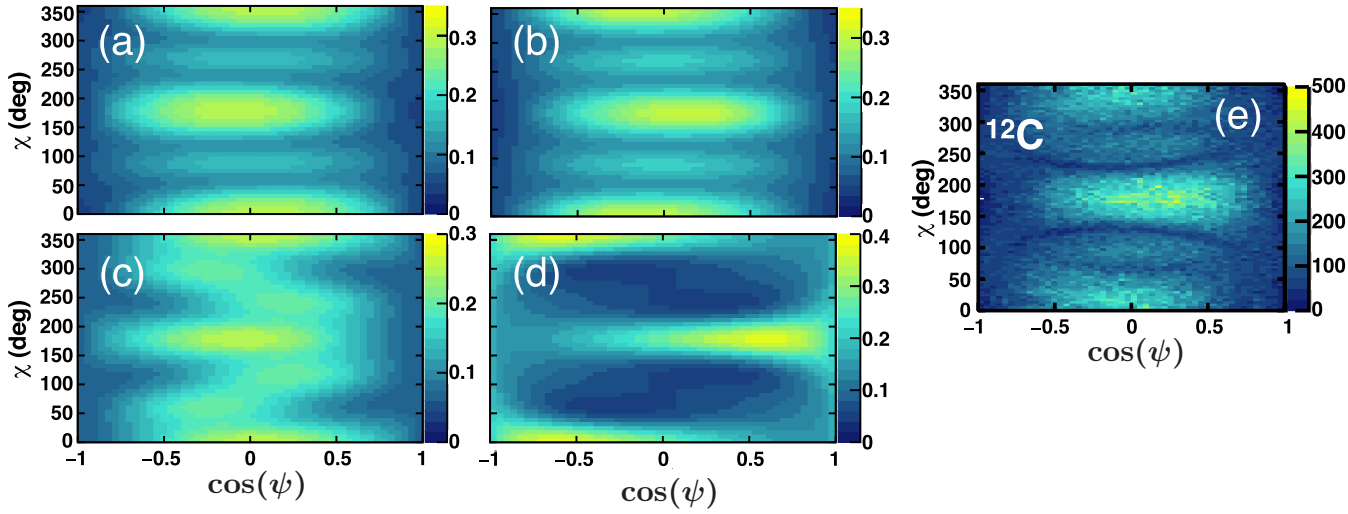

FIG. 8. Angular correlations from DWBA cluster-model calculations of ^{7}Li* [4.63 MeV] breakup after interaction with a ^{12}C target, which remains in its ground state, with: (a) no spin-orbit term, (b) $V_{\rm SO} = 0.55$ and $W_{\rm SO} = 0.72$ MeV, (c) $V_{\rm SO} = 3.0$ MeV and $W_{\rm SO} = 0.72$, and (d) $V_{\rm SO} = 0.55$ MeV and $W_{\rm SO} = 1.44$. (e) For comparison, the measured angular correlations for the breakup of ^{7}Li* after interacting with the ^{12}C target.

to the ground state of ^{16}F ($J^{\pi} = 0^{-}$) [24]. At sufficiently high beam-energies, the first proton is preferentially emitted perpendicular to the beam-axis, indicating large longitudinal spin alignment of ^{17}Ne* [25]. This observation of alignment illustrates that the alignment mechanism outlined is not a consequence of cluster structure.

Using the same breakup model and optical-model potential parameters for ^{7}Li (changing the fragment and core for each case), DWBA calculations were performed for the inelastic excitations to particle-decaying states of ^{6}Li, ^{17}Ne, and ^{7}Be at the appropriate experimental energies ($E/A = 36.6$, 58.5, and 65.5 MeV, respectively) and angular regions [13,24,25]. The experiments show, and the calculations predict, that the alignment produced is fairly constant above the grazing angle. However, the calculations indicate that transverse alignments must be present at small scattering angles due to the inclusion of the spherical harmonics Y_0^L in the wave function. Indeed at $\theta_{\rm c.m.} = 0^{\circ}$, the only contribution to the alignment is from $M = 0$ (no tilting), and thus $m_f = m_i$ meaning no longitudinal alignment is possible. The green dashed lines

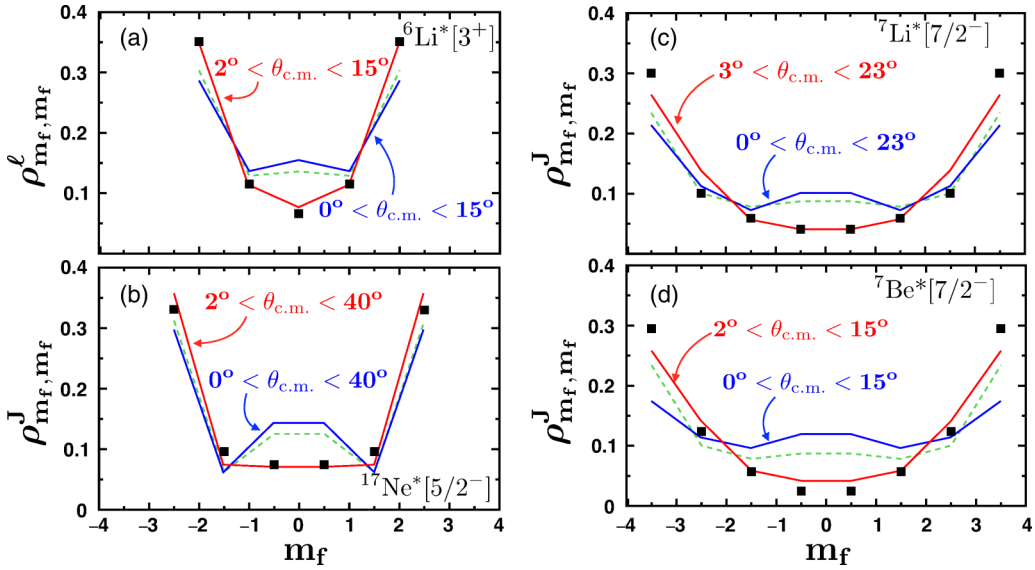

FIG. 9. Magnetic-substate distributions extracted from the data (solid squares) and predicted by DWBA (lines) for single inelastic excitation to particle-decaying states in (a) ^{6}Li, (b) ^{17}Ne, (c) ^{7}Li, and (d) ^{7}Be. Note for (a) ^{6}Li the magnetic substate distribution is for the decay angular momentum ($\ell_{\rm decay} = 2$). The blue and red solid lines are the DWBA predictions for angular regions including and excluding small angles, respectively. The green dashed lines are predictions from the Clebsch-Gordan coefficients in Eq. (16), omitting the energy and angle dependence. The black squares are data from this and other works.

in Fig. 9 correspond to the squared T matrix predictions from Eq. (16) for a single L (equal to L_{graz}) and omitting the angle and implicit energy dependence. These lines are in remarkable agreement with the solid blue line obtained from the T matrix integrated over the entire angular region. If small-angle scattering is removed, the T matrix calculations (solid red lines) show significant enhancement to the alignment due to the suppression of $M = 0$ transitions (non-tilting). This feature of the alignment mechanism was observed for ^{7}Be [13]. The experimental magnetic-substate distributions for ^{6}Li$^{*}[3^{+}]$, ^{7}Li$^{*}[7/2^{-}]$, ^{17}Ne$^{*}[5/2^{-}]$, and ^{7}Be$^{*}[7/2^{-}]$ are shown as black squares in Fig. 9. The data for ^{6}Li, ^{17}Ne, and ^{7}Be are from Refs. [13,25]. The agreement between the data and the DWBA predictions, excluding small angles, is remarkable for several of the cases, and demonstrates the limited acceptance of the detector arrays for small angles. There is a small discrepancy in the predicted alignment for ^{7}Be. Although the optical potential parameters found for ^{7}Li + ^{12}C should be more reasonably suited for the ^{7}Be + ^{9}Be system than the other presented systems (since the projectiles are isobaric analogs), the ^{7}Be experiment was performed at a much larger beam energy ($E/A = 65.5$ MeV) and so the phenomenological optical potentials used may not be as representative of the ^{7}Be + ^{9}Be system due to the implicit energy dependence of the potentials.

It should be noted that the predictions and data for ^{6}Li* in Fig. 9 are for magnetic-substate populations of the decay channel angular momentum. In principle, one can reconstruct the final angular momentum state, J_f, from the relationship $J_f = \ell_{\text{decay}} + s_{\text{core}} + s_{\text{frag}}$, assuming there is only one decay channel angular momentum. However, only systems where $s_{\text{core}} = 0$ and $s_{\text{frag}} = 1/2$, or vice-versa, are completely constrained and allow for the extraction of $\rho^{J}_{m_f,m_f}$. In the ^{6}Li case, the measured magnetic-substates of the decay angular momentum indicate large longitudinal alignment, but the magnetic-substate populations of the excited projectile cannot be extracted. This is made clear by repeating the density matrix analysis in Ref. [13] for the ^{6}Li case ($J_f = 3, \ell_{\text{decay}} = 2, s_{\text{core}} = 0, s_{\text{frag}} = 1$) resulting in the set of equations,

$$\rho^{\ell}_{2,2} = \rho^{J}_{3,3} + \tfrac{1}{3}\rho^{J}_{2,2} + \tfrac{1}{15}\rho^{J}_{1,1}, \tag{17}$$

$$\rho^{\ell}_{1,1} = \tfrac{2}{3}\rho^{J}_{2,2} + \tfrac{8}{15}\rho^{J}_{1,1} + \tfrac{1}{5}\rho^{J}_{0,0}, \tag{18}$$

$$\rho^{\ell}_{0,0} = \tfrac{4}{5}\rho^{J}_{1,1} + \tfrac{3}{5}\rho^{J}_{0,0}. \tag{19}$$

There is no fully constrained solution for the final magnetic-substate populations for J given the measurement of magnetic-substate populations for ℓ_{decay}. If ^{6}Li decayed with a smaller ℓ_{decay}, then almost no alignment information would be recoverable.

A. Predictions for ^{12}C + ^{12}C

The ^{12}C + ^{12}C system is simpler than ^{7}Li + ^{12}C as there are no spin-spin or spin-orbit interactions. Extensive studies measuring the spin alignment of a single 2^{+} [4.44 MeV] inelastic excitation of ^{12}C have been performed at low energies [6,9,26]. These studies were focused on correlating gross structures in the alignment with intermediate structures in the excitation function of the reaction cross section. While no strong correlation was found, these studies were consistent with the reduction

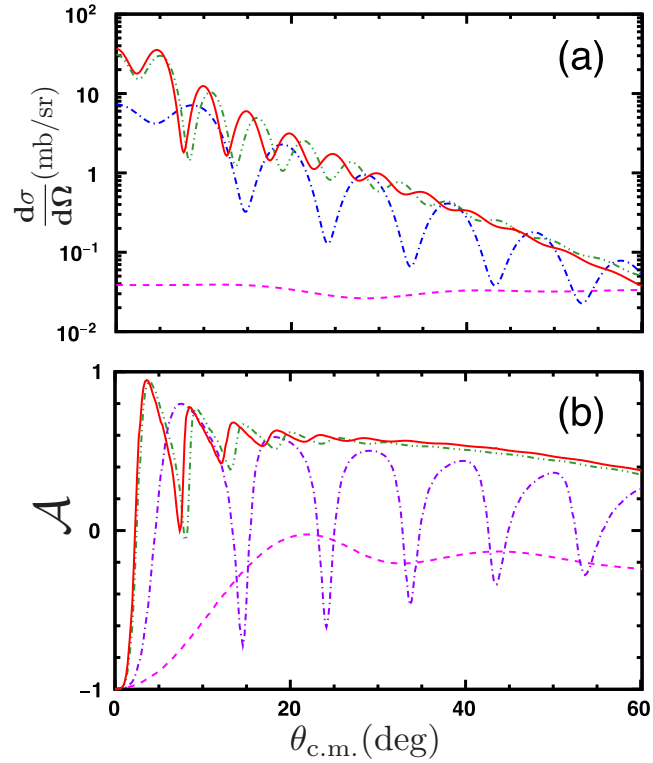

FIG. 10. (a) Differential cross sections for the single inelastic excitation of ^{12}C* [4.44 MeV] predicted by a DWBA soft-rotator model for the beam energies $E/A = 2.0$, 5.8, 12.0, and 17.0 MeV (purple dashed, blue dot-dashed, green dot-dot-dashed, and red solid line, respectively). (b) A coarse excitation function of the spin alignment for ^{12}C*, as a function of scattering angle, for the same beam energies.

in magnitude of the incoming partial wave by $2\hbar$. Furthermore, these studies suggest the reaction is dominated by only one incoming partial wave due to molecular-like resonances in the experimental energy regime. Without the smoothing effect produced by a range of partial waves, a single partial wave will produce large oscillations in the alignment with angle. To effectively measure the gross structure in alignment (because of these oscillations) the alignment measurements need to be angle-averaged and weighted by the differential cross section [9]. All of the previously mentioned studies restricted themselves to center-of-mass angles $\theta_{\text{c.m.}} > 30^{\circ}$, and thus a large portion of the reaction yield, and resulting alignment, was missed.

Even still, the transfer of angular momentum generated in the reaction to the intrinsic spin of ^{12}C* is consistent with the alignment mechanism outlined in this work, and at larger beam energies tilting of the exit-channel reaction plane should occur resulting in a longitudinal spin alignment of ^{12}C*. Predictions for the spin alignment of ^{12}C* [4.44 MeV] have been made previously using a variety of models including DWBA predictions [27], but these studies focused on the previously mentioned low-energy data sets.

The proposed alignment mechanism can be tested by measuring a coarse excitation function of the generated spin

alignment as a function of scattering angle. These measurements would allow one to probe the predicted threshold of the alignment mechanism. By measuring the spin alignment over a large portion of the reaction yield (i.e., scattering angles around the grazing angle) the gross structure of the alignment can be found and compared to theoretical predictions. Figure 10(a) shows the differential cross sections predicted by a DWBA soft-rotator model for the beam energies $E/A = 2.0$, 5.8, 12.0, and 17.0 MeV (purple dashed, blue dot-dashed, orange dot-dot-dashed, and red solid line, respectively), while Fig. 10(b) shows the corresponding alignments. The optical-potential parameters employed came from the literature [28]. To do a proper phenomenological optical-model analysis, the optical potential parameters should be fit to differential elastic and inelastic cross section data at each energy because of the implicit energy dependence of phenomenological optical potentials.

Well below the angular-momentum-excitation-energy mismatch threshold, around $E/A = 5$ MeV (deduced from semiclassical calculations), the overall alignment should be transverse to the beam axis ($\mathcal{A} < 0$). This is predicted for measurements at a beam energy of $E/A = 2.0$ MeV. Larger longitudinal alignment should be observed after passing this threshold (this is seen for the $E/A = 5.8$ MeV prediction in Fig. 10). Interestingly, the minima in the alignment correspond with diffraction minima in the differential scattering cross section. This a consequence of the fact that the same spherical harmonics are responsible for the diffraction minima in the differential cross section and angular distributions for the alignment. Further, these minima in alignment will not be observed in the angle-averaged alignment because it is weighted by the differential cross section. Well above this threshold, the generated alignment does not vary significantly with energy (comparing $E/A = 12.0$ and 17.0 MeV) and the gross structure of alignment should be similar to the Clebsch-Gordan coefficients in Eq. (16). Also, the contribution of many partial waves to the cross section result in a spin alignment that is fairly constant at large scattering angles. Since the overall yield of the alignment has to be weighted by the differential cross section, the overall (i.e., gross) alignment will be largely longitudinal at intermediate energies.

VII. CONCLUSION

We have found large longitudinal spin alignment of ^{7}Li* produced in single inelastic excitations with targets of C, Be, and Al. Large longitudinal spin alignment has also been observed in several other particle-unbound systems. These observations are explained by an alignment mechanism stemming from an angular-momentum-excitation-energy mismatch. Above a certain beam-energy threshold, which depends on the excitation energy and change in fragment spin, the reaction-plane is forced to tilt to conserve angular momentum. The ^{7}Li + ^{12}C reaction studied, where ^{7}Li is excited to the $J^{\pi} = 7/2^{-}$[4.63 MeV] state and ^{12}C remains in its ground state, is well characterized by DWBA calculations and suggest the reaction is purely a nuclear transition. DWBA calculations are consistent with the semiclassical argument for tilting of the exit-channel reaction plane and predict longitudinal alignment to be present in single inelastic excitations of many nuclear systems. The effect of spin-orbit coupling on the alignment produced is discussed, and it was found that angular correlation measurements, along with differential cross section data, can put constraints on the strength of these spin-orbit effects. With the observation of longitudinal alignment generated by an angular-momentum-excitation-energy mismatch in systems where a cluster-model is inappropriate, it is clear that this alignment phenomenon is more general and should also apply to Coulomb excitation as well. The proposed alignment mechanism may be the primary mechanism for large longitudinal alignments already utilized in g-factor measurements at intermediate energies [4].

ACKNOWLEDGMENTS

This experiment would not have been possible were it not for the loan of the upstream Si detector from Dirk Rudolph, the downstream Si detector from Jason Burke, and a mating CsI(Tl) array for the latter from Romualdo deSouza. This work was supported by the U.S. Department of Energy, Division of Nuclear Physics under Grants No. DE-FG02-87ER-40316 and No. DE-FG02-93ER-40773. K.W.B. was supported by the National Science Foundation Graduate Research Fellowship under Grant No. DGE-1143954.

[1] K. Sekiguchi, H. Sakai, H. Witała, W. Glöckle, J. Golak, M. Hatano, H. Kamada, H. Kato, Y. Maeda, J. Nishikawa *et al.*, Phys. Rev. C **65**, 034003 (2002).
[2] F. Schmidt, R. E. Brown, J. Gerhart, and W. A. Kolasinski, Nucl. Phys. **52**, 353 (1964).
[3] J. J. Kolata and A. Galonsky, Phys. Rev. **182**, 1073 (1969).
[4] A. D. Davies, A. E. Stuchbery, P. F. Mantica, P. M. Davidson, A. N. Wilson, A. Becerril, B. A. Brown, C. M. Campbell, J. M. Cook, D. C. Dinca *et al.*, Phys. Rev. Lett. **96**, 112503 (2006).
[5] P. F. Mantica, A. E. Stuchbery, D. E. Groh, J. I. Prisciandaro, and M. P. Robinson, Phys. Rev. C **63**, 034312 (2001).
[6] S. J. Willett, S. K. Korotky, R. L. Phillips, D. A. Bromley, and K. A. Erb, Phys. Rev. C **28**, 1986 (1983).
[7] J. J. Kolata, R. Auble, and A. Galonsky, Phys. Rev. **162**, 957 (1967).
[8] A. E. Stuchbery, Nucl. Phys. A **723**, 69 (2003).
[9] W. Trombik, W. Trautmann, F. Krug, W. Dünnweber, D. Konnerth, W. Hering, R. Singh, and D. Zeppenfeld, Phys. Lett. B **135**, 271 (1984).
[10] Z. Majka, D. G. Sarantites, L. G. Sobotka, K. Honkanen, E. L. Dines, L. A. Adler, L. Ze, M. L. Halbert, J. R. Beene, D. C. Hensley *et al.*, Phys. Rev. Lett. **58**, 322 (1987).
[11] A. H. Wuosmaa, R. W. Zurmühle, P. H. Kutt, S. F. Pate, S. Saini, M. L. Halbert, and D. C. Hensley, Phys. Rev. C **41**, 2666 (1990).
[12] N. Kato, K. Anai, T. Tachikawa, H. Fujita, K. Kimura, T. Sugimitsu, and Y. Nakajima, Phys. Lett. B **120**, 314 (1983).

[13] R. J. Charity, J. M. Elson, J. Manfredi, R. Shane, L. G. Sobotka, Z. Chajecki, D. Coupland, H. Iwasaki, M. Kilburn, J. Lee *et al.*, Phys. Rev. C **91**, 024610 (2015).
[14] D. E. M. Hoff, R. J. Charity, K. W. Brown, C. D. Pruitt, L. G. Sobotka, T. B. Webb, G. Potel, B. Roeder, and A. Saastamoinen, Phys. Rev. Lett. **119**, 232501 (2017).
[15] D. Brink, Phys. Lett. B **40**, 37 (1972).
[16] J. F. Ziegler, J. P. Biersack, and U. Littmark, *The Stopping and Range of Ions in Solids* (Pergamon Press, New York, 1985); the code SRIM can be found at www.srim.org.
[17] Y. Ichikawa, H. Ueno, Y. Ishii, T. Furukawa, A. Yoshimi, D. Kameda, H. Watanabe, N. Aoi, K. Asahi, D. L. Balabanski *et al.*, Nat. Phys. **8**, 918 (2012).
[18] W.-D. Schmidt-Ott, K. Asahi, Y. Fujita, H. Geissel, K.-D. Gross, T. Hild, H. Irnich, M. Ishihara, K. Krumbholz, V. Kunze *et al.*, Z. Phys. A **350**, 215 (1994).
[19] G. R. Satchler, Nucl. Phys. **55**, 1 (1964).
[20] W. Nörenberg and H. Weidenmüller, *Introduction to the Theory of Heavy-Ion Collisions* (Springer, New York, 1976).
[21] I. J. Thompson, Comput. Phys. Rep. **7**, 167 (1988).
[22] C. M. Perey and F. G. Perey, At. Data Nucl. Data Tables **17**, 1 (1976).
[23] O. B. Tarasov and D. Bazin, Nucl. Instrum. Meth. Phys. Res. Sect. B **266**, 4657 (2008).
[24] K. W. Brown, R. J. Charity, J. M. Elson, W. Reviol, L. G. Sobotka, W. W. Buhro, Z. Chajecki, W. G. Lynch, J. Manfredi, R. Shane *et al.*, Phys. Rev. C **95**, 044326 (2017).
[25] R. J. Charity *et al.*, Phys. Rev. C (to be published).
[26] D. P. Balamuth, L. E. Cannell, and R. W. Zurmühle, Phys. Rev. C **23**, 2492 (1981).
[27] O. Tanimura and U. Mosel, Phys. Lett. B **114**, 7 (1982).
[28] I. Kohno, J. Phys. Soc. Jpn. **38**, 945 (1975).